Adaptive inverse control for the pickup head flying height of near-field optical disk drives

Adaptive inverse control for the pickup head flying height of near-field optical disk drives

C C Hsiao, T S Liu[1] and S H Chien

Department of Mechanical Engineering, National Chiao Tung University, Hsinchu 30010,
Taiwan, Republic of China

E-mail: tsliu@mail.nctu.edu.tw

Abstract
Near-field optical disk drives represent a promising technique for optical data
recording to achieve an even larger storage density and capacity than
DVD-ROM and Blu-ray disk drives. To realize near-field optics, unlike
conventional optical disk drives, a flying pickup head is required. In this
study, the pickup head consists of a suspension arm, a slider and a bimorph
piezoelectric bender between the suspension arm and the slider. The dynamic
model of the pickup head is identified using measurement, but the whole
dynamics including both pickup head and interface dynamics between the
disk and slider is unmodeled. Adaptive inverse control of robustness is
developed to track the vibratory deformation of rotating optical disks, so that
the flying height of a pickup head can remain stable in the presence of
modeling error. Experimental results demonstrate that using the proposed
method the pickup head can not only track disk deformation but also
maintain the flying height.

(Some figures in this article are in colour only in the electronic version)

1. Introduction

The storage capacity of optical disk drives has been increasing
in the past decade. Although nowadays high density optical
storage media like DVD disks and Blu-ray are available, people
are still attempting to find a revolutionary way to record a
dramatically increased number of data. Near-field optical disk
drives (NFODD) represent one potential device [1, 2], for
which a capable servo system must be constructed to facilitate
reading and writing. Yatsui *et al* [3] used a pyramidal silicon
probe on a slider to perform near-field recording and reading.
Kurita *et al* [4] adjusted the flying height for a magnetic
head slider using a piezoelectric micro-actuator. To achieve
high precision in focusing for near-field data recording, it is
essential to develop servo systems that can maintain a constant
height at which the pickup head flies above a rotating disk.
Hence in this work we attach a bimorph piezoelectric (PZT)
bender to the suspension of a slider to compensate for the

surface deformation of rotating optical disks. To control the
flying height, the PZT bender bends under an applied voltage
to maintain a constant height between a rotating disk and
the pickup head. However, the PZT bender has inherent
hysteresis nonlinearity which will cause imprecision when
using conventional linear controllers.

Ge and Jouaneh [5] presented a tracking control approach
for a piezoelectric actuator, incorporating a feedforward loop
with a feedback controller. Zhou *et al* [6] dealt with a
piezohydraulic actuator with a hybrid model consisting of a
dynamic part and a static nonlinear part. Takaishi *et al* [7]
developed a dual-stage controller composed of a voice coil
motor and a PZT for precise position tracking.

Owing to the time-varying and nonlinear properties
inherent in piezoelectric materials, a robust controller is needed
to achieve high accuracy and a fast operating speed. Besides,
the dynamics between the pickup head and the rotating disk is
hard to obtain in practice. It is impossible for most controllers
to achieve high accuracy since the overall system dynamics is
unmodeled. Thus, in this paper adaptive inverse control (AIC)

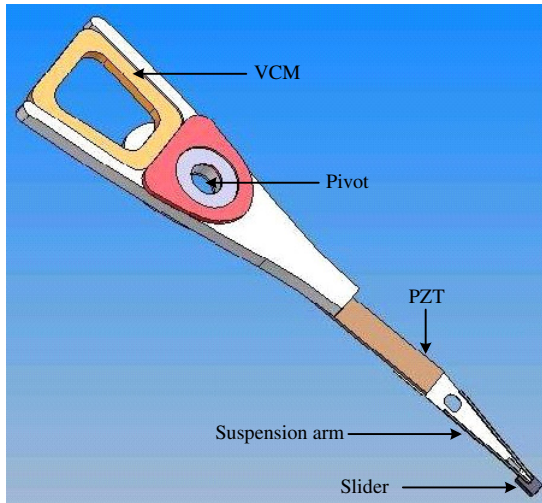[1] Author to whom any correspondence should be addressed.

Figure 1. Pickup head including the PZT bender.

Figure 2. Bode plot of the pickup head.

Figure 3. Bode plot of the pickup head after compensation.

is developed to achieve accurate motion control in NFODD. Plett [8] presented AIC for unmodeled linear systems. Kaelin and von Grunigen [9] proposed an approach to decreasing computational complexity and accelerating convergence rate by splitting AIC controllers into a long fixed and a short adaptive filter. Widrow and Plett [10] proposed feedforward control for both linear and nonlinear plant.

In this paper, section 2 introduces the PZT characteristics and identifies the mathematical model of a pickup head. In section 3, an adaptive inverse controller is developed to control the flying height of the pickup head. Experimental results and conclusions are presented in sections 4 and 5, respectively.

2. Pickup head identification

PZT elements have been widely applied as actuators in addition to sensors, and their performance is qualified to generate fast and precise movement. Among various PZT actuators, PZT benders are popular in many structural applications, such as individual blade control in rotorcraft, vibration dampening and positional control. Since a large deformation of the disk surface during disk rotation may well degrade focusing performance in near-field disk drives, in the present pickup head a PZT bender attached to a suspension arm, as shown in figure 1, serves as an actuator to maintain the flying height in the presence of vibratory disk deformation.

In this study, a swept-sine method is employed to obtain the dynamic characteristics of the pickup head, and hence its Bode plot, from which a transfer function is determined. As a result, the model of the pickup head is identified as

$$G_p(s) = \{1.779 \times 10^8 s^2 + 2.055 \times 10^{10} s$$
$$+ 1.886 \times 10^{15}\}\{s^4 + 1203 s^3 + 1.047 \times 10^8$$
$$+ 2.657 \times 10^{10} + 4.235 \times 10^{14}\}^{-1}. \quad (1)$$

At sampling time $T_s = 0.0001$ s, equation (1) can be written in discrete form

$$G_p(z) = \frac{0.7935 z^3 - 0.7306 z^2 - 0.656 z + 0.7557}{z^4 - 2.965 z^3 + 3.877 z^2 - 2.762 z + 0.8867}. \quad (2)$$
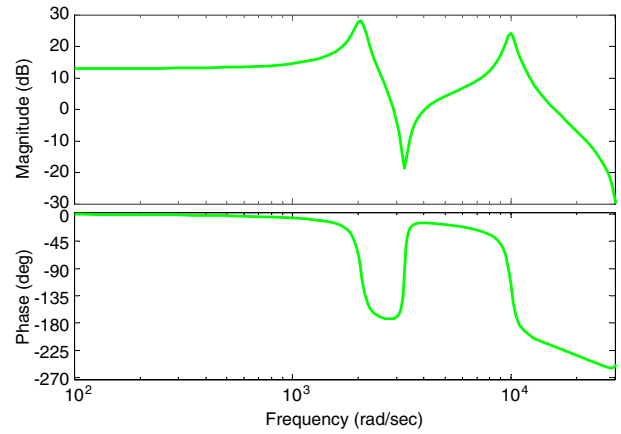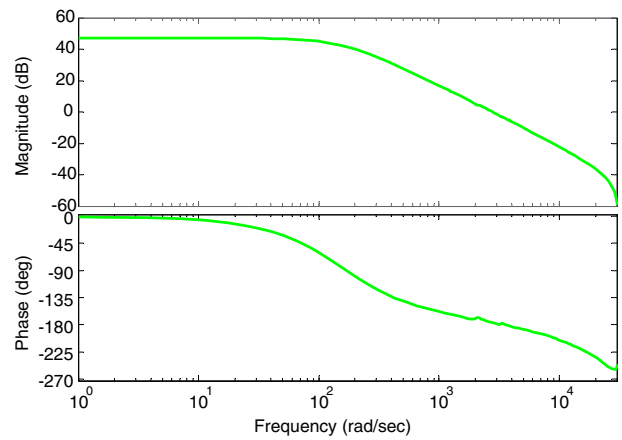
Its Bode plot is depicted in figure 2, where resonances at 2000 and 10 000 rad s^{-1} exist. Hence, a compensator is designed to filter out the resonances. Cascading the compensator with the pickup head and utilizing feedback network results in a system with better dynamics. The compensator is designed as

$$C_p(z) = \{0.05(z - 0.9233)(z^2 - 1.027 z + 0.9057)$$
$$\times (z^2 - 1.938 z + 0.9794)\}\{(z - 0.9)$$
$$\times (z^2 - 1.883 z + 0.9878)(z^2 - 1.97 z + 0.9702)\}^{-1}. \quad (3)$$

It consists of proportional-integral (PI) control and two notch filters, which aim to suppress both resonances. The Bode plot of the compensated system is depicted in figure 3, where both resonances have been suppressed. Figure 2 depicts the dynamics of the pickup head, but it does not represent the whole system dynamics. The whole system dynamics should include the dynamics of the pickup head and the interface dynamics between the disk and slider; i.e. the air bearing effect. Therefore, the whole system dynamics is unmodeled. Although the pickup head model $G_p(z)$ does not include the air bearing effect, in this study the air bearing effect is treated as a disturbance and will be taken into account in the process of modeling AIC.
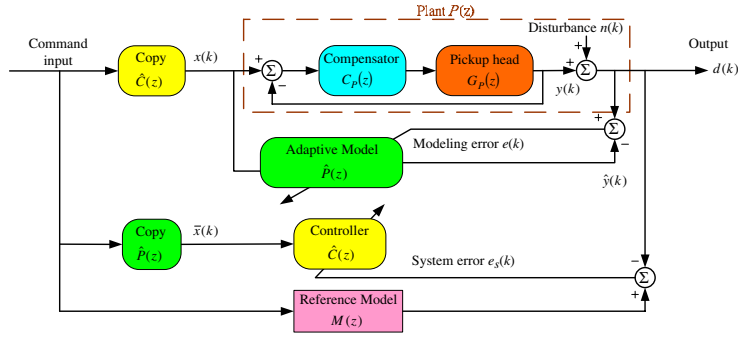
Figure 4. Adaptive inverse control.

3. Adaptive inverse control

AIC is robust and adjusts itself to optimize the overall dynamic response. It is implemented by using an adaptive filter containing a tapped delay line with adjustable parameters. Parameters are adjusted to minimize a least mean square (LMS) error function. Figure 4 depicts the block diagram of AIC [11], which consists of two main parts: one is adaptive modeling, i.e. nonlinear identification, and the other is inverse control. With good adaptive modeling, an LMS based algorithm can be used to train the AIC controller. Based on the LMS algorithm in minimizing the mean square error, adaptive modeling aims to estimate the model of the real plant.

3.1. Adaptive modeling

As depicted in figure 4, the transfer function of a plant is $P(z)$ whose output is $y(k)$. A discrete-time additive disturbance $n(k)$ appears at the output where the discrete time index is k. The overall measured output is $d(k)$, given by

$$d(k) = y(k) + n(k). \tag{4}$$

The impulse response of the adaptive model $\hat{P}(z)$ in the vector form is written as

$$\hat{P}(z) = [\hat{p}_1 \ \hat{p}_2 \cdots]^{\mathrm{T}}. \tag{5}$$

The adaptive model $\hat{P}(z)$ yields an output response $\hat{y}(k)$, being the convolution of its input signal with its impulse response:

$$\hat{y}(k) = x(k) * \hat{p}(k). \tag{6}$$

The adaptive model $\hat{P}(z)$ is an estimation of the plant $P(z)$ aiming to yield a response $\hat{y}(k)$ as close as possible to $d(k)$. The plant $P(z)$ consists of pickup head model $G_{\mathrm{p}}(z)$, its compensator $C_{\mathrm{p}}(z)$ and disturbance $n(k)$. Taking the z-transform for equation (6) gives

$$\hat{Y}(z) = X(z)\hat{P}(z). \tag{7}$$

Parameters in the adaptive model $\hat{P}(z)$ are adjusted by adaptive algorithms to minimize the modeling error $e(k)$ in the sense of the mean square error. Defining a performance function called J_{ms}, the mean square error is written as

$$J_{\mathrm{ms}} = E\left\{e^2(k)\right\} \tag{8}$$

where $E\{\cdot\}$ denotes an expectation operator. Minimizing the mean square error leads to

$$J_{\mathrm{ms}} \cong J_{\mathrm{min}}. \tag{9}$$

The minimization procedure [12] using the mean square error will be described in the next subsection.

3.1.1. Least mean square. The objective of the adaptive model $\hat{P}(z)$ is to find an optimal weighting W^0 that minimizes the performance function J, the expected value of the square error. Defining the modeling error as

$$e(k) = d(k) - \hat{y}(k) \tag{10}$$

the performance function can be written as

$$\begin{aligned} J &= E\left\{e^2(k)\right\} = E\left\{d(k) - \hat{y}(k)\right\}^2 \\ &= E\left\{d^2(k)\right\} - 2E\left\{d(k) \cdot \hat{y}(k)\right\} + E\left\{\hat{y}^2(k)\right\}. \end{aligned} \tag{11}$$

Since

$$\hat{y}(k) = \sum_{l=0}^{N-1} x(k-l)w_l = X^{\mathrm{T}}(k)W, \tag{12}$$

where N is the number of weights and

$$X(k) = [x(k)x(k-1)x(k-2)\cdots x(k-N+1)]^{\mathrm{T}} \tag{13}$$

$$W = [w_0 \ w_1 \cdots w_{N-1}]^{\mathrm{T}}. \tag{14}$$

Equation (11) can be rewritten as

$$\begin{aligned} J &= E\left\{d^2(k)\right\} - 2W^{\mathrm{T}} E\left\{d(k)X(k)\right\} \\ &\quad + W^{\mathrm{T}} E\left\{X(k)X^{\mathrm{T}}(k)\right\} W^*. \end{aligned} \tag{15}$$

For convenience, we define the expected power of $d(k)$ as

$$D \cong E\left\{d^2(k)\right\}. \tag{16}$$

The ensemble autocorrelation matrix of $x(k)$ is expressed by

$$R \cong E\left\{X(k)X^{\mathrm{T}}(k)\right\}. \tag{17}$$

The ensemble average cross-correlation vector is written as

$$P \cong E\left\{d(k)X(k)\right\}. \tag{18}$$

To make D, P and R time invariant, $d(k)$ and $x(k)$ are assumed stationary, in a wide sense. Accordingly,

$$J = D - 2W^{\mathrm{T}}P + W^{\mathrm{T}}RW. \qquad (19)$$

An optimal weighting is found when

$$\nabla_{\mathrm{w}}J = -2P + 2RW \cong 0. \qquad (20)$$

This leads to

$$W^0 = R^{-1}P. \qquad (21)$$

In such an optimal condition, the performance function in equation (19) is a minimum; i.e.

$$J_{\min} = D - 2W^{0^{\mathrm{T}}}P + W^{0^{\mathrm{T}}}RW^0 = D - W^{0^{\mathrm{T}}}P. \qquad (22)$$

Let W be the actual weighting, related to the optimal weighting W^0 by

$$W = W^0 + V. \qquad (23)$$

Substituting equations (22) and (23) into equation (19) yields

$$J = J_{\min} + V^{\mathrm{T}}RV \qquad (24)$$

i.e. if $V = W - W^0 \cong 0$, the performance function will be minimized. With recursive training, this can indeed be done. Nevertheless, some stability conditions must be satisfied to guarantee convergence.

3.1.2. FIR filter based on the gradient descent approach.

A gradient descent approach to finding the optimal weighting is expressed by

$$W(k+1) = W(k) - \mu\nabla_{\mathrm{w}}J|_{W=W(k)} \qquad (25)$$

where μ represents the updating step size. Different from equation (20), differentiation of equation (24) yields another form of gradient

$$\nabla_{\mathrm{w}}J = 2RV. \qquad (26)$$

We define

$$R = Q\Lambda Q^{-1} \qquad (27)$$

$$\Lambda = \mathrm{diag}\,[\,\lambda_1 \quad \lambda_2 \quad \cdots \quad \lambda_N\,] \qquad (28)$$

where Λ denotes an eigenvalue matrix of R in a diagonal form, and Q is a N-by-N matrix, formed by eigenvectors of R. We define a transformed version of V as

$$V = QV'. \qquad (29)$$

Equally, the transformation equation (29) can be applied to the weight vector

$$W = QW'. \qquad (30)$$

Accordingly, equation (24) becomes

$$J = J_{\min} + V'^{\mathrm{T}}\Lambda V'. \qquad (31)$$

Using equations (23), (26), (27) and (31), equation (25) becomes

$$V'(k+1) = (I - 2\mu\Lambda)\,V'(k). \qquad (32)$$

Solving the difference equation (32) gives

$$V'(k) = (I - 2\mu\Lambda)^k V'(0) \qquad (33)$$

$$V'(0) = W'(0) - W^{0\prime}(0) \qquad (34)$$

where $V'(0)$ is an initial condition. To ensure convergence in equation (33), the step size μ is chosen such that

$$|1 - 2\mu\lambda_i| < 1, \qquad \text{for } 1 \leqslant i \leqslant N. \qquad (35)$$

Therefore, the condition for stability of the weight vector is

$$0 < \mu < \frac{1}{\lambda_{\max}} \qquad (36)$$

where $\lambda_{\max}$ is the largest eigenvalue of R.

3.2. Adaptive inverse controller

Figure 4 depicts an AIC strategy [11], where the training signal of the controller $\hat{C}$ is the system error signal $e_{\mathrm{s}}(k)$, i.e. the reference model output minus the actual system output $d(k)$, not from the modeling error signal $e(k)$. Even if $\hat{P}(z)$ is truncated and is not a perfect match to $P(z)$, the adaptive algorithm will tend to minimize the overall system error by optimizing the choice of $\hat{C}(z)$. It is noted that adaptation is still active when the plant $P(z)$ is identified by the adaptive modeling process. Hence, this ensures that AIC can adjust itself and further control the whole system when the system is affected by the air bearing and nonlinear properties inherent in piezoelectric materials.

To explain how the forward controller copy $\hat{C}(z)$ serves as an 'inverse control' to achieve AIC, we focus on the lower part in figure 4. Cascading the model copy $\hat{P}(z)$ and controller $\hat{C}(z)$ can be treated as an open-loop transfer function. The output $\bar{x}(k)$ of both copy $\hat{P}(z)$ and system error $e_{\mathrm{s}}(k)$ act as updating signals to optimize the parameters of the controller $\hat{C}(z)$ and further eliminate system error $e_{\mathrm{s}}(k)$ based on the LMS algorithm. Once the system error $e_{\mathrm{s}}(k)$ is eliminated, the open-loop transfer function equals the reference model $M(z)$, which can be expressed as

$$\hat{P}(z) \cdot \hat{C}(z) = M(z). \qquad (37)$$

Since the adaptation only updates parameters in controller $\hat{C}(z)$, we rewrite equation (37) as

$$\hat{C}(z) = M(z) \cdot \frac{1}{\hat{P}(z)} \qquad (38)$$

where controller $\hat{C}(z)$ is expressed as a product of the reference model $M(z)$ and the inverse of the adaptive model $\hat{P}(z)$.

The forward path at the top of figure 4 cascades the copy $\hat{C}(z)$ and plant $P(z)$ (after adaptive modelling $\hat{P}(z)$ substitutes for $P(z)$), and the open-loop transfer function relating the command input $x(k)$ and system output $\hat{y}(k)$ is written as

$$\frac{\hat{Y}(z)}{X(z)} = \hat{C}(z) \cdot \hat{P}(z) = M(z). \qquad (39)$$

The reference model $M(z)$ is chosen to have the same dynamic response that the designer wants for the system. Hence, adaptive modeling aims to estimate the real plant based on the LMS algorithm to eliminate modeling error $e(k)$. Once the adaptive model $\hat{P}(z)$ can be estimated by the adaptive modeling process, an inverse controller $\hat{C}(z)$ can be obtained from equation (38) and used to eliminate system error $e_{\mathrm{s}}(k)$. After convergence, cascading the copy $\hat{C}(z)$ and the plant $P(z)$ results in the same dynamic response as the reference model does.

4. Experimental results

The experimental setup consists of a PC, two laser Doppler vibrometers that respectively generate a single laser beam for displacement sensing, two A/D–D/A cards that receive two displacement signals sensed by two laser Doppler vibrometers, the pickup head and PZT amplifier, and near-field optical disks,
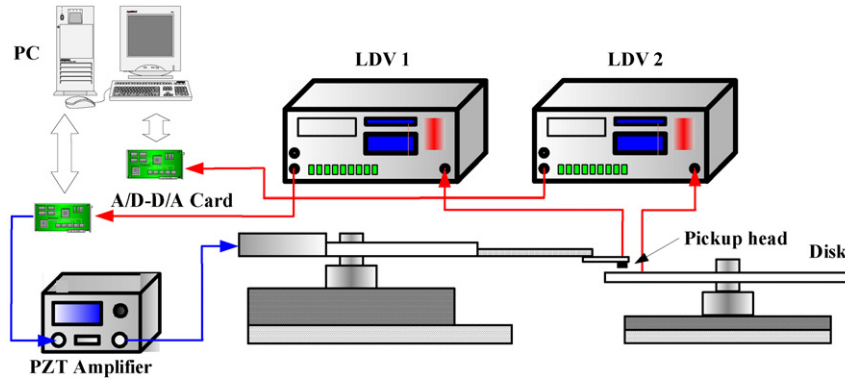
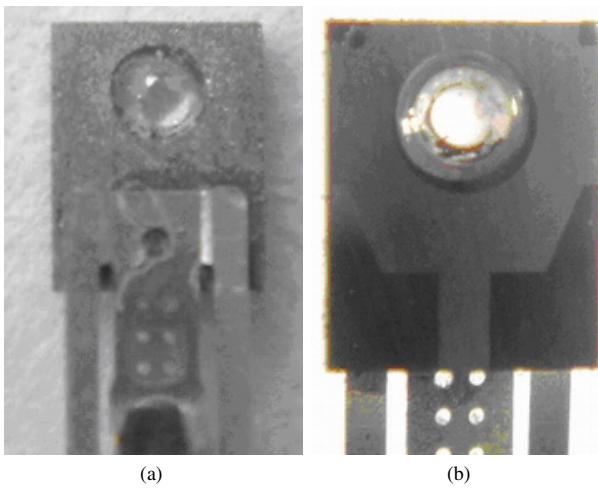**Figure 5.** Experimental setup using dual-laser beams to sense the pickup head and disk displacements.

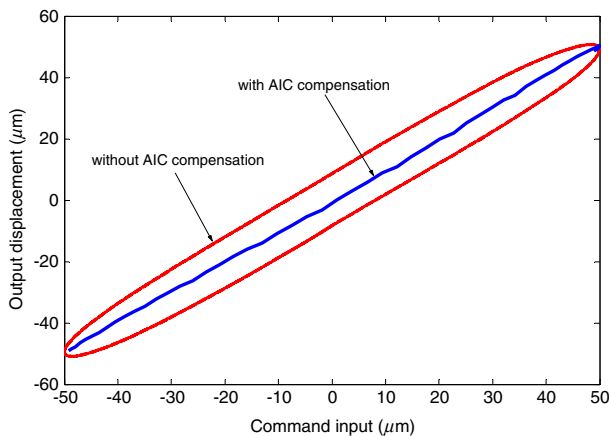**Figure 6.** Photograph of the slider: (a) top, (b) bottom.

Figure 7. Hysteresis loops for 50 μm with and without compensation.

Figure 8. Hysteresis loops for 5 μm with and without compensation.

as depicted in figure 5. The control method is mastered by a PC that receives both the disk displacement signal and the pickup head displacement signal via two A/D–D/A cards. The PC generates a driving signal calculated by AIC via a D/A converter and a signal amplifier to control the pickup head
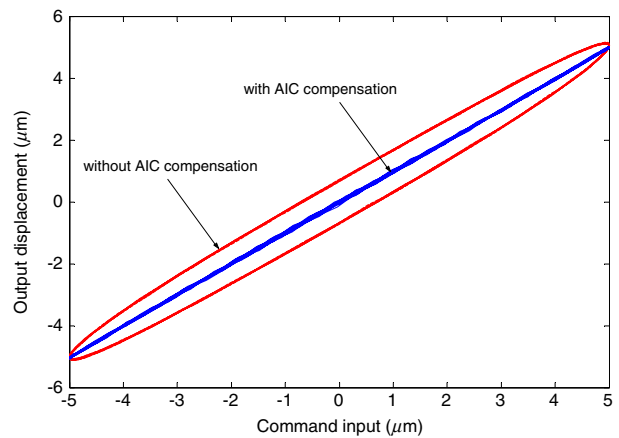
displacement. In experiments the sampling rate is 10 kHz and the disk rotation speed is 5400 rpm. Figures 6(a) and (b) show the top and bottom photographs of the slider, respectively.

AIC can be separated into two main procedures in experiments. Adaptation for the plant $P(z)$ should be done ahead of adaptive inverse control. It is desired to obtain $\hat{P}(z)$ as close as possible to $P(z)$. The adaptive model $\hat{P}(z)$ chosen as FIR form with a weight vector W of 100 elements in adaptation for the plant model $P(z)$. The adaptive algorithm employs the LMS method, but is modified as a normalized LMS of the form [13]

$$W(k+1) = W(k) + \mu e(k) X(k) \tag{40}$$

$$\mu(k) = \frac{\alpha}{\gamma + X^{\mathrm{T}}(k) X(k)} \tag{41}$$

where α and γ are set as 0.004 and 1, respectively. Rather than constant step sizes, the step size function $\mu(k)$ in normalized LMS is time varying and is updated by the input signal $X(k)$. The step size $\mu(k)$ automatically shrinks or enlarges according to the product of $X^{\mathrm{T}}(k) \cdot X(k)$. Parameters in the adaptation and adaptive algorithm of controller $\hat{C}(z)$ are the same as in the adaptive modeling process. A pure delay model usually results in good performance control. Here, the reference model $M(z)$ is chosen to be a delay of 20 samples. AIC in experiments employs the LMS algorithm
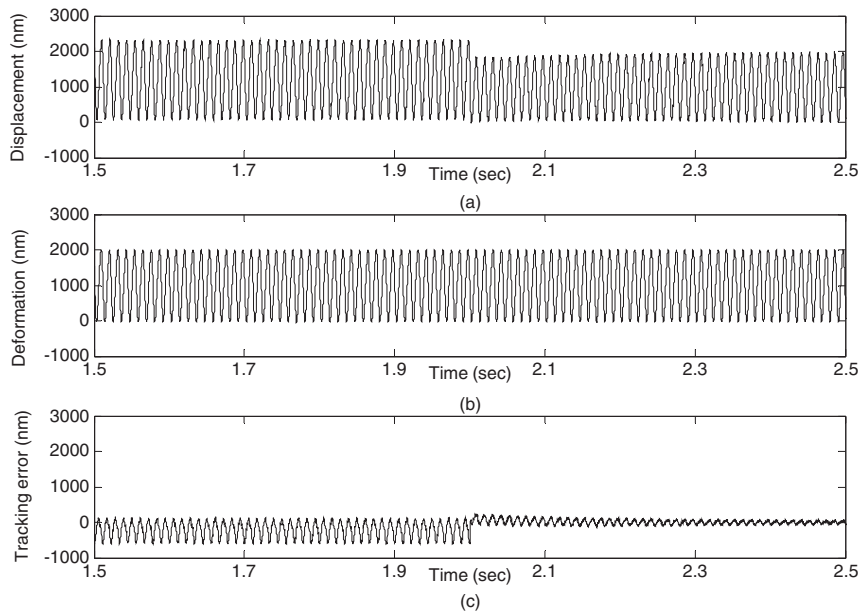
Figure 9. Pickup head tracks 2 μm disk deformation: (a) pickup head displacement, (b) disk deformation, (c) tracking error.
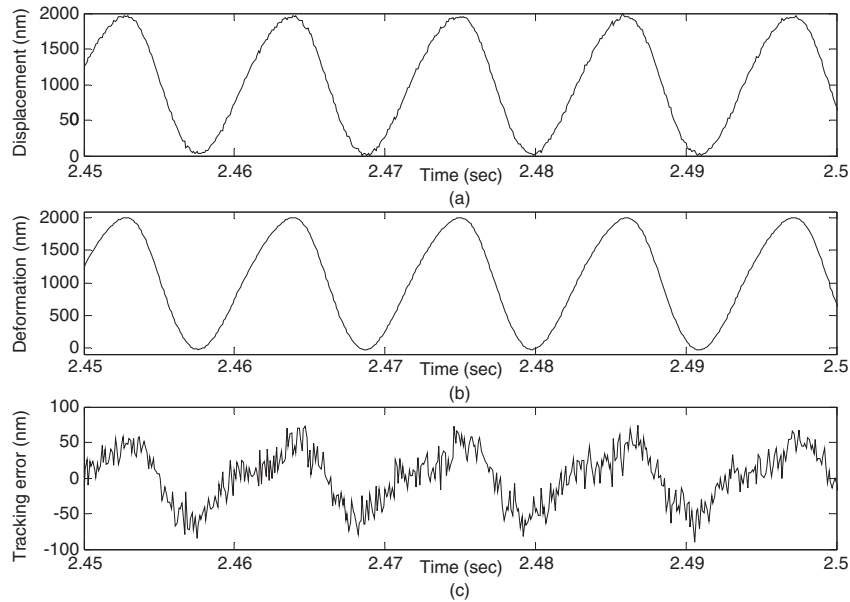

Figure 10. Enlarged view in figure 9 from 2.45 to 2.5 s.

to save computational time. Adaptive modeling is performed before 2 s, while AIC is carried out after 2 s. From 0 and 2 s, AIC only drives the PZT bender without control by using a training signal so as to capture plant dynamics $P(z)$ and further obtain an adaptive model $\hat{P}(z)$. After 2 s, AIC indeed controls the pickup head to track the command input.

4.1. Hysteresis compensation

The hysteresis property of the PZT bender causes imprecision in tracking, for which hysteresis compensation is undertaken by using AIC. The hysteresis properties of the PZT bender cause 15% imprecision. Hence, hysteresis compensation is

necessary for AIC to control the displacement of the pickup head. Figures 7 and 8, respectively, compare experimental hysteresis loops for 50 and 5 μm with and without AIC. In figure 7, the hysteresis is reduced by 90% by using AIC. In figure 8, using AIC the hysteresis loop shrinks to become a straight line.

4.2. Tracking disk deformation

To demonstrate the control method in compensating for disk deformation, the pickup head tracks a real disk deformation of 2 μm. Figures 9 and 10 depict results of an experiment in which the pickup head tracks 2 μm disk deformation.
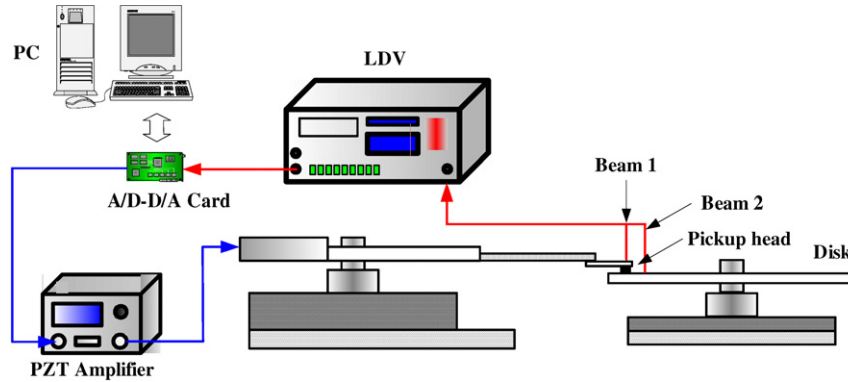
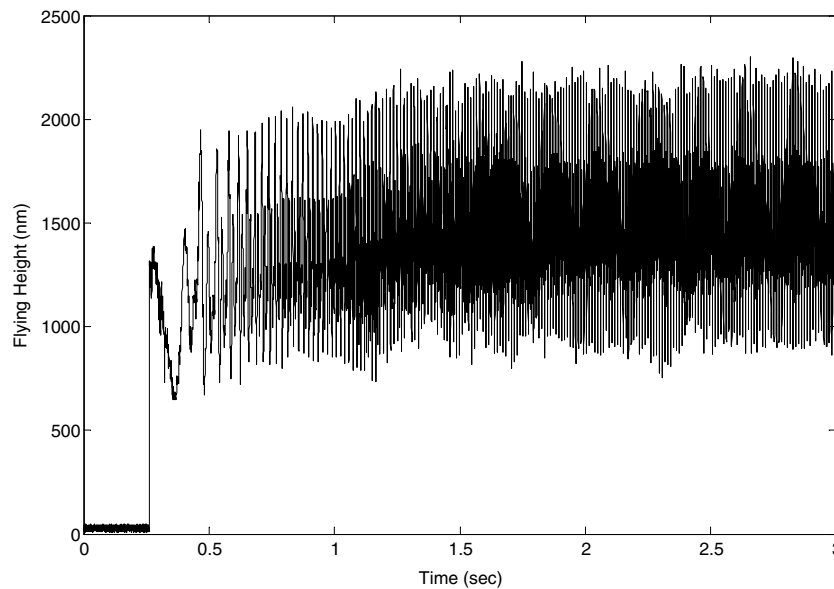**Figure 11.** Experimental setup using a dual-beam laser to sense the flying height.

Figure 12. Free-flying height without AIC control.

Figures 9(a) and (b) respectively depict the pickup head displacement and disk deformation, while figure 9(c) depicts the corresponding tracking error. Figure 10 enlarges figure 9 from 2.45 and 2.5 s. The tracking error lies between ±50 nm, which is 5% of the disk deformation. Experimental results verify that with AIC the pickup head can efficiently track disk deformation.

4.3. Measurement of flying height

Another experimental setup depicted in figure 11, different from figure 5, is used to measure the flying height of the pickup head. The present experiment uses only one laser Doppler vibrometer that generates both laser beams 1 and 2 focusing on the slider and the disk surface, respectively.

Figure 12 depicts the flying height of the pickup head without AIC control. Figures 13(a) and (b) enlarge figure 12 from 0.25 to 0.35 and 2 to 2.1 s, respectively. The slider takes off from disk surface at 0.262 s and flies stably after 2 s between 900 and 2200 nm. According to the measurement results, the flying height can be measured by

using the experimental setup depicted in figure 11, which will be employed in subsequent experiments on control of flying height.

4.4. Flying height control

Two experimental cases are presented for control of flying height.

Case 1: Desired average flying height 1650 nm. Figure 14(a) depicts histories of control of flying height by the AIC controller when the desired average flying height is set at 1650 nm. The AIC controller is turned on and starts at 6 s and error converges at 9 s. Figures 14(b) and (c) are enlarged views from 5 to 5.1 and 9 to 9.1 s, respectively. In figure 14(b) the flying height varies between 3000 and 1500 nm, and the average flying height is 2250 nm. In figure 14(c), the average flying height is $(1900 + 1400)/2 = 1650$ nm and the variation in the flying height reduces to $1900 - 1400 = 500$ nm. The AIC controller lowers the average flying height by $2250 - 1650 = 600$ nm and reduces the measured variation of the flying height by 67%.
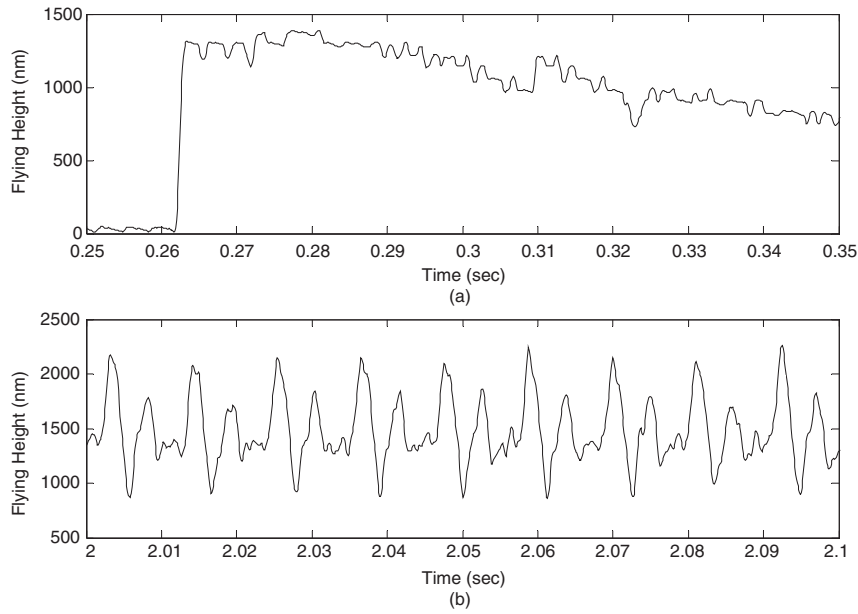
Figure 13. Enlarged view of figure 12 from (a) 0.25 to 0.35 s, (b) 2 to 2.1 s.
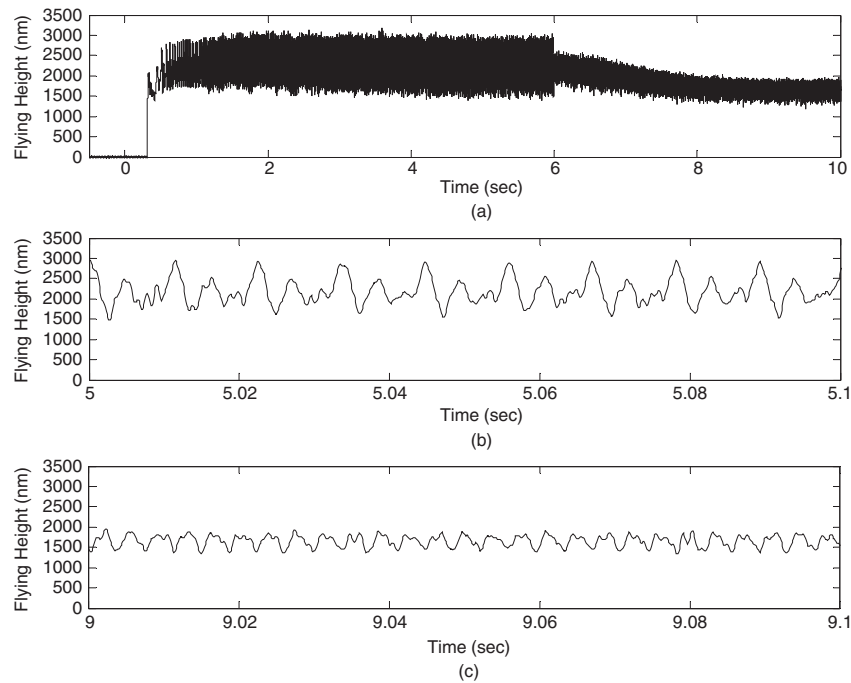

Figure 14. (a) Control history for a desired average flying height of 1650 nm. (b) Enlarged view from 5 to 5.1 s. (c) Enlarged view from 9 to 9.1 s.

Case 2: Desired average flying height 800 nm. Figure 15(a) depicts histories of control of flying height using AIC when the desired flying height is set at 800 nm. Figures 15(b) and (c) are enlarged views from 5 to 5.1 and 9 to 9.1 s, respectively. In figure 15(b) the flying height varies between 2800 and 1100 nm and the average flying height is 1950 nm. In figure 15(c), the average flying height is $(1100 + 500)/2 = 800$ nm and the variation in the flying height reduces to $1100 - 500 = 600$ nm. The AIC controller

lowers the average flying height by $1950 - 800 = 1150$ nm and reduces the variation in measured flying height by 65%.

5. Conclusion

To maintain a stable flying height of the pickup head, a novel pickup head is presented to meet the demands of near-field optical disk drives. A PZT bender serves as an actuator to track the vibratory deformation of the disk surface. However, unmodeled system dynamics results in
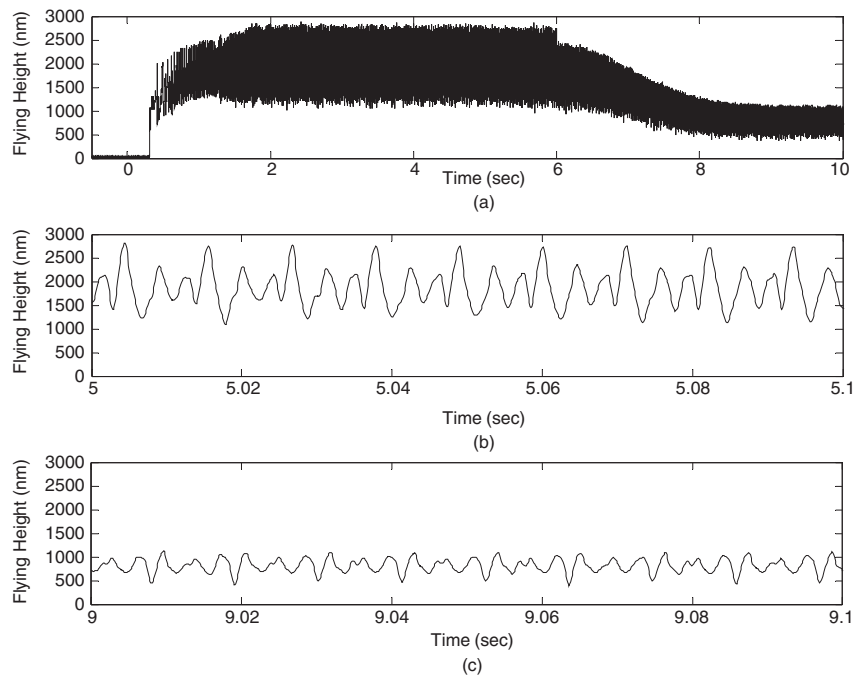
Figure 15. (a) Control history for a desired average flying height of 800 nm. (b) Enlarged view from 5 to 5.1 s. (c) Enlarged view from 9 to 9.1 s.

difficulty in controlling the flying height. AIC is very suitable for controlling the unmodeled system dynamics due to its robustness. This study has carried out experiments using AIC to effectively compensate for hysteresis and track disk deformation. Moreover, this study has sensed and controlled the flying height of the pickup head.

Acknowledgment

References

[1] Lee J H, Oh H R, Gweon D G, Jung H and Jeong J 2004 Optical flying head mounted on four-wire type actuator *Sensors Actuators* A **113** 100–5

[2] Mizuno T, Kojima N, Hitosugi T, Sako K and Watanase K 2004 An optical configuration based on flying head structure for near-field recording *Japan. J. Appl. Phys.* **43** 1403–9

[3] Yatsui Y, Kourogi M, Tsutsui K, Ohtsu M and Takahashi J I 2000 High-density-speed optical near-field recording–reading with a pyramidal silicon probe on a contact slider *Opt. Lett.* **25** 1279–81

[4] Kurita M, Tsuchiyama R, Tokuyama M, Xu J, Yoshimura Y, Kohira H, Su L and Kato K 2003 Flying-height adjustment of a magnetic head slider with a piezoelectric micro-actuator *IEEE Trans. Magn.* **39** 2480–2

[5] Ge P and Jouaneh M 1996 Tracking control of a piezoceramic actuator *IEEE Trans. Control Syst. Technol.* **4** 209–16

[6] Zhou Q, Kallio P and Koivo H N 1999 Modeling of a piezohydraulic actuator for control of a parallel micromanipulator *Proc. IEEE Int. Conf. Rob. Autom.* pp 2750–5

[7] Takaishi K, Imamura T, Mizoshita S and Ueno, Yamada T 1996 Microactuator control for disk drive *IEEE Trans. Magn.* **32** 863–6

[8] Plett G L 2002 Adaptive inverse control of unmodeled stable SISO and MIMO linear systems *Int. J Adapt. Control Signal Process* **16** 243–72

[9] Kaelin A and von Grunigen D 2000 On the use of *a priori* knowledge in adaptive inverse control *IEEE Trans. Circuits Syst.* I **47** 54–62

[10] Widrow B and Plett G L 1996 Adaptive inverse control based on linear and nonlinear adaptive filtering *Proc. Int. Workshop Neur. Networks Identif. Control Rob. Sign. Ima. (Venice, Italy)* pp 30–8

[11] Widrow B and Walach E 1995 *Adaptive Inverse Control* (Upper Saddle River, NJ: Prentice-Hall)

[12] Treichler J R, Johnson C R and Larimore M G 2001 *Theory and Design of Adaptive Filters* (Upper Saddle River, NJ: Prentice-Hall)

[13] Bilcu R C, Kuosmanen P and Egiazarian K 2002 A transform domain LMS adaptive filter with variable step-size *IEEE Signal Process. Lett.* **9** 51–3